



# Cardiac endocardial left atrial substrate and lesion depth mapping using near-infrared spectroscopy

SOO YOUNG PARK,<sup>1</sup> HAIQIU YANG,<sup>1</sup> CHARLES MARBOE,<sup>2</sup> OHAD ZIV,<sup>3</sup> KENNETH LAURITA,<sup>3,4</sup> ANDREW ROLLINS,<sup>4</sup> DEEPAK SALUJA,<sup>5</sup> AND CHRISTINE P. HENDON<sup>1,\*</sup>

<sup>1</sup>Department of Electrical Engineering, Columbia University, New York, USA

<sup>2</sup>Department of Cell Biology and Pathology, Columbia University Irving Medical Center, New York, USA

<sup>3</sup>Department of Medicine, Cardiology Division, MetroHealth Hospital, Ohio, USA

<sup>4</sup>Department of Biomedical Engineering, Case Western Reserve University, Ohio, USA

<sup>5</sup>Department of Medicine, Cardiology Division, Columbia University Irving Medical Center, New York, USA

\*[cpf2115@columbia.edu](mailto:cpf2115@columbia.edu)

**Abstract:** Atrial fibrillation (AF) is a rapid irregular electrical activity in the upper chamber and the most common sustained cardiac arrhythmia. Many patients require radiofrequency ablation (RFA) therapy to restore sinus rhythm. Pulmonary vein isolation requires distinguishing normal atrial wall from the pulmonary vein tissue, and atrial substrate ablation requires differentiating scar tissue, fibrosis, and adipose tissue. However, current anatomical mapping methods for strategically locating ablation sites by identifying structural substrates in real-time are limited. An intraoperative tool that accurately provides detailed structural information and classifies endocardial substrates could help improve RF guidance during RF ablation therapy. In this work, we propose a 7F NIRS integrated ablation catheter and demonstrate endocardial mapping on *ex vivo* swine ( $n = 12$ ) and human ( $n = 5$ ) left atrium (LA). First, pulmonary vein (PV) sleeve, fibrosis and ablation lesions were identified with NIRS-derived contrast indices. Based on these key spectral features, classification algorithms identified endocardial substrates with high accuracy ( $<11\%$  error). Then, a predictive model for lesion depth was evaluated on classified lesions. Model predictions correlated well with histological measurements of lesion dimensions ( $R = 0.984$ ). Classified endocardial substrates and lesion depth were represented in 2D spatial maps. These results suggest NIRS integrated mapping catheters can serve as a complementary tool to the current electroanatomical mapping system to improve treatment efficacy.

© 2022 Optica Publishing Group under the terms of the [Optica Open Access Publishing Agreement](#)

## 1. Introduction

Pulmonary vein isolation with radiofrequency ablation (RFA) treatment is a common therapy for patients with atrial fibrillation [1]. RFA therapy is a minimally invasive procedure that uses heat create lesions to create condition block within arrhythmogenic tissue. Anatomically, many have identified ectopic foci to be initiated from the pulmonary vein sleeves [2,3]. Thus, isolation of focal discharges originating near the pulmonary vein (PV) is the first cardinal step to treat atrial fibrillation. However, 20-50% of patients require repeat ablation procedures from AF recurrences following initial procedure [4–6]. In persistent atrial fibrillation, complex atrial substrate may exist beyond pulmonary veins, potentially limiting the effectiveness of PV isolation alone [7]. Left atrial tissue structure is complex due to substrate heterogeneity, with the possible presence of scar, fibrosis, collagen and adipose tissue. Although the underlying process of AF remains unclear, clinical studies have identified atrial fibrosis as a major contributing factor for persistent AF recurrences [8–10]. Also, AF recurrences can occur due to incomplete ablation. Insufficient

thermal treatment allows conduction recovery, which ultimately permits AF resurgence. In addition, overtreatment can result in adverse consequences. The quality of RF energy delivery in areas of initiating foci and arrhythmogenic substrates is directly correlated to treatment success [11]. Therefore, effective treatment is predicated in part on identifying triggers and complex substrates for strategic RF lesion placement, and isolating or eliminating them with complete, transmural lesions.

Current ablative approaches for treating AF have low efficacy in part by inability to locate and isolate arrhythmogenic substrates. Prior to ablation, the left atrium is rendered in 3D with an electroanatomic mapping (EAM) system using a diagnostic catheter to first identify important anatomical locations, particularly around the veno-atrial junctions [12]. After anatomical reconstruction, atrial arrhythmogenic regions are analyzed by measuring electrogram characteristics. Low voltage areas are branded as locations of potential arrhythmogenic substrate [13]. It has been reported that patients with low voltage areas shown on EAM bioelectrical measurements have higher probability of AF recurrences due to diseased atrial substrate [14]. PVs are then isolated with circumferential RF ablation and in some patients, arrhythmogenic substrate is ablated. Recently, lesion sufficiency was predicted by correlation of ablation parameters, such as power, contact force, temperature, time, impedance [11,15–17]. However, these are indirect methods to estimate lesion progression, and it is not possible to estimate lesion sufficiency when ablation sites are revisited. Therefore, a technique to discern structural complexities, such as pulmonary vein and atrial fibrosis real-time, and validate lesion sufficiency at the catheter tip after ablation could enhance understanding AF structural substrates and treatment success.

Previously, several groups have identified cardiac structural substrates using various imaging modalities. Conventional computed tomography (CT) and magnetic resonance (MR) imaging have quantified left atrial fibrosis substrates and detection of scar following AF ablation [6,7,18,19]. However, MR is costly and CT does not provide real-time data analysis. Hyperspectral autofluorescence imaging uses ultraviolet light to excite the tissue surface and study the emitted light within the visible range [20–22]. Lesion locations have been clearly shown by analyzing spectral differences under ultraviolet light, but lesion transmural and areas of other tissue structures have not been identified with hyperspectral imaging yet. Optical coherence tomography (OCT) is a high-resolution optical imaging modality, which enables 3D volume acquisition with 1–2mm imaging penetration depth. OCT has been shown to distinguish cardiac substrates and has been used to classify myocardium, adipose, fibrotic tissue, and RF treated tissue [23–30]. Fiber based OCT also enables 1mm imaging penetration depth and has enabled imaging of collagen and lesions in detail [31,32]. However, the extent of tissue necrosis has not been evaluated due to OCT's inherent depth limitations, and a strength of photoacoustics technology [33,34].

Near-infrared spectroscopy (NIRS) enables assessment of pathological tissue by analyzing light interaction within tissue optical properties using near-infrared light. Recently, our group proposed a parameter to distinguish adipose in human epicardium and estimated epicardial fat thickness with a 12F NIRS-integrated catheter [35]. Also, an endoscopic NIR multispectral imaging system was developed to classify pulmonary veins, untreated and non-irrigated RF treated tissue in swine left atrium [36]. For lesion assessment, several groups have employed NIRS to assess non-irrigated lesion depth [37–40]. Previously, our group demonstrated tracking of non-irrigated lesion up to 4mm and irrigated lesion, *in vivo* [40,41]. However, simultaneous identification of structural substrate and irrigated lesion sufficiency using NIRS has not been demonstrated yet. In this work, we introduce a NIRS-integrated RF dual diagnostic/ablation catheter and demonstrate real-time endocardial structural substrate and lesion depth mapping on *ex vivo* swine and human hearts. A classification algorithm is proposed with NIRS derived contrast parameters as inputs to identify four structural substrates within the human model: normal tissue, pulmonary vein sleeve, irrigated lesions, and fibrosis. Additionally, we propose a model to estimate irrigated lesion depth percentage with a set of parameters called lesion optical

indices (LOI) [41]. Lastly, NIRS-predicted structural substrates were compared with bench-top OCT 3D volumes to explore advantages of using both modalities for future studies.

## 2. Methods

### 2.1. Optical catheter construction

Figure 1 illustrates a schematic diagram of the NIRS-integrated RFA mapping catheter. Two multimodal fibers are integrated into a commercial open-tip irrigated Celsius thermocool RFA catheter (DI7TCDLRT, Biosense Webster, Diamond Bar, CA). The catheter is capable of monitoring irrigated RF ablation in real-time and mapping tissue substrate. The outer diameters of the detection fiber and the illumination fiber are  $250\mu\text{m}$  and  $320\mu\text{m}$ , respectively. The distance between the two fibers was fixed at 0.9 mm. A detailed description of the system has been previously described [40] and is briefly described below. The source fiber is connected to a broadband light source (HL-2000HP, Ocean Optics Inc, Dunedin, FL) and illuminates the tissue surface. The detection fiber collects diffusely backscattered light, which is then analyzed by the spectrometer (600-1000 nm) (C9405CB, Hamamatsu, Bridgewater, NJ). All measurements were recorded at 50hz on a laptop computer and processed in MATLAB (The Mathworks Inc., Natick, MA).

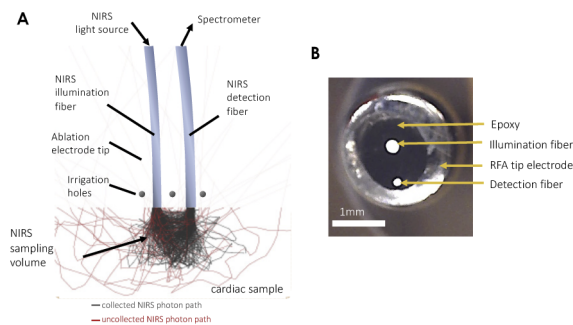


**Fig. 1.** Combined NIRS mapping and radiofrequency ablation catheter. A: An illustration of NIRS mapping catheter within commercial ablation catheter and its important features. B: NIRS catheter distal tip shows two multimodal optical fibers integrated inside commercial RFA catheter.

### 2.2. Experimental protocol

A total of 12 healthy swine hearts were acquired within 24 hours of sacrifice (Green Village Packing Co., Green Village, NJ). In addition, 5 human donor hearts were acquired from National Disease Research Interchange (NDRI). All specimens were de-identified and not considered as human subjects research, according to the Department of Health and Human services human subject regulation exemption 4 and Columbia University's Institutional Review Board under 45 CFR 46. The inclusion criteria for the NDRI protocol includes end stage heart failure, cardiomyopathy, coronary heart disease, amyloid, atrial fibrillation, and myocardial infarction. Table 1 describes a summary of donors' medical histories and causes of death. All hearts were procured by NDRI within 24 hours after death. Donor hearts #4 and #5 had missing left pulmonary veins from initial procurement upon arrival to the lab. All experiments were conducted within 24 hours of arrival. For each heart, the left atrial sample was segmented with pulmonary veins intact. Then, a longitudinal cut was made along the largest pulmonary vein and into the LA to open up the vein. Three swine hearts were mapped with NIRS prior to ablation to evaluate the ablation-induced changes. For each heart, the dissected LA was

submerged in a temperature-maintained ( $37^{\circ}\text{C}$ ) phosphate buffered saline (PBS) flowing bath. Using our NIRS-integrated ablation catheter, irrigated lesions were generated with a commercial RF generator (Stockert 70, Biosense Webster, USA). Target power and ablation time settings were varied from 15-35W and 15-45s, respectively, and the saline irrigation system (CoolFlow, Biosense Webster, USA) settings were maintained at 10, 13, and 17 ml/min, which are flow rates adapted from clinical ablation settings [42]. The range of ablation settings allowed for the generation of lesions of a variety of sizes. Lesions were targeted near the PV junctions to replicate pulmonary vein isolation lesions. A total of 72 lesions with varying dimensions were generated on swine left atrial samples. A total of 31 lesions were created on human left atrial specimens. Following RF ablation, left atrial tissue was flattened and pinned onto a corkboard and PBS solution was applied. All hearts were mapped immediately after completing RF ablation sets. After mapping, histological analysis of all samples were carried out as detailed below in section 2.4.

**Table 1. Donor Hearts Medical Information <sup>a</sup>**

Heart #	Age	Sex	BMI	Disease History	Cause of Death
1	44	F	27.30	HTN, SVT, S, AF, CM	Vascular Collapse
2	67	F	36.69	HTN, MI, DM, AS	CA
3	66	M	48.73	AF, HTN, PVD, CAD, DVT, DJD, G	Anoxia
4	49	M	23.13	HTN, MI, CA, CHD, CHF, E, G	Cardiovascular
5	29	F	32.07	CAD, HTN, S	S

<sup>a</sup>AF - HTN - hypertension; CVA - cerebrovascular Accident; SVT - supraventricular tachycardia; AF - atrial fibrillation; CM - cardiomyopathy; CA - cardiac arrest; CAD - coronary artery disease; MI - myocardial infarction; DM - diabetes type 2; AS - Aortic stenosis; PVD - peripheral vascular disease; DJD; Degenerative joint disease; DVT - deep vein thrombosis; G - gout; E - endocarditis; CHD - congenital heart defect; CHF - congestive heart failure; S - stroke;

The experiment flow chart is shown in Fig. 2. Prior to NIRS mapping, a reference image of each flattened left atrial sample was taken to co-register with camera-tracked sampled locations. Then, NIRS optical measurements were obtained under a camera-based tracking configuration, where a CCD camera (Thorlabs, NJ) tracks the catheter tip. Custom MATLAB software was used to track catheter tip and co-register with the reference image. The number of total NIRS optical measurements in a single atrium ranged from 200-600 points. NIRS-derived parameters, explained in the following section, were co-registered at each measured site and mapped onto the reference image. These sites were interpolated using a natural neighbor interpolation scheme over a structured grid and enclosed by the convex hull. All processing was performed in MATLAB.

### 2.3. NIRS signal processing and contrast parameters

NIRS measurements were calibrated and converted into relative reflectance ( $R_{\text{rel}}$ ), following a previously published protocol [44]. Briefly, the calibration process includes dark current subtraction, instrumental response subtraction, normalization using titanium dioxide ( $\text{TiO}_2$ ), and silicone phantom measurement of known optical properties. With healthy swine hearts, NIRS contrast parameters for pulmonary vein, lesion, and normal myocardium were derived based on spectral morphology Fig. 3(A) shows mean  $R_{\text{rel}}$  spectra of lesion, pulmonary vein, and normal myocardium. Lesion  $R_{\text{rel}}$  spectra show an overall elevation in the 700-900nm range. Compared to normal myocardium, a slight decrease at 650nm followed by a large elevation until 710nm is observed in ablated tissue. This was emphasized in the derivative of  $R_{\text{rel}}$  ( $R'_{\text{rel}}$ ) as it revealed a maximum at 680nm and a minimum at 950nm (Fig. 3(B)). The mean  $R_{\text{rel}}$  value of pulmonary vein exhibited a relatively linear slope with a dip at 950nm, which was observed in all three classes. Based on these observations, we formed two parameters called lesion optical index (LOI)

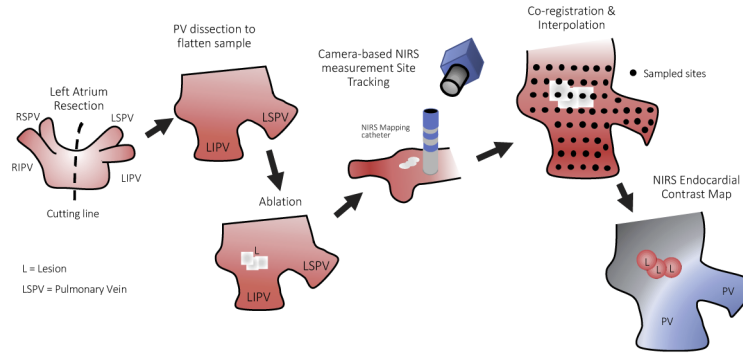


**Fig. 2.** Experimental flow diagram of human endocardial substrate mapping. First, the dissected left atrium is cut in half and longitudinal cuts are made along the pulmonary vein sleeves to flatten the sample. Then, irrigated lesions are generated near the PVs. Optical measurements are acquired under the camera-based tracking system. Position tracked measurement sites are co-registered and interpolated to generate NIRS endocardial contrast maps.

and pulmonary vein optical index (PVOI). These parameters are stated below.

$$LOI = \sum_{\lambda_1}^{\lambda_2} |R'_{Rel}(\lambda) - R'_{Rel}(952nm)|, [\lambda_1, \lambda_2] = [660nm, 690nm] \quad (1)$$

$$PVOI = \frac{R_{Rel}(630nm)}{R_{Rel}(670nm)} \quad (2)$$

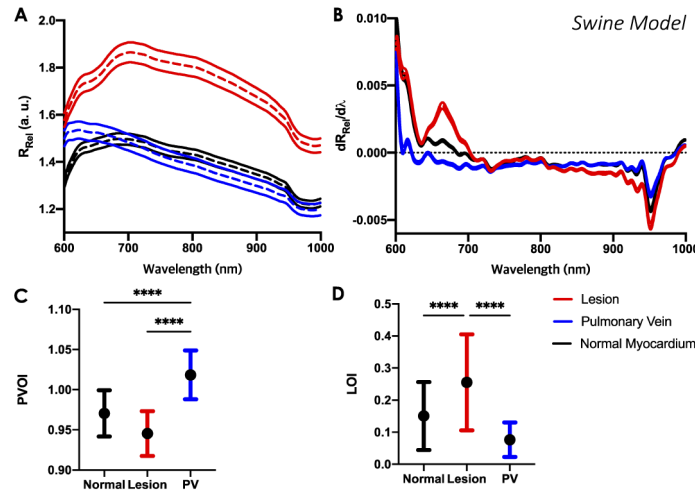


**Fig. 3.** Spectral morphology assessment of swine substrates. A: mean (dotted line) and 95% confidence interval (line) relative reflectance ( $R_{Rel}$ ) of pulmonary vein, normal myocardium and lesion. B: The first derivative of the  $R_{Rel}$  curve to highlight changes in spectral morphology. C: Pulmonary vein optical index (PVOI) comparison between substrates. PVOI is described as follows:  $R_{Rel}(630nm)/R_{Rel}(670nm)$ . D: Lesion optical index (LOI) comparison between identified substrates. LOI is described as follows:  $\sum_{\lambda_1}^{\lambda_2} |R'_{Rel}(\lambda) - R'_{Rel}(952nm)|, [\lambda_1, \lambda_2] = [660nm, 690nm]$ . Bars are presented as mean and standard deviation (\*\*\*\* $P < 0.0001$ ).



LOI highlights  $R_{Rel}$  slope changes observed between 660 nm and 690 nm (Fig. 3(A)) and area under the curve around the peak shown in  $R'_{Rel}$ . LOI showed statistical significance between lesion and the other two classes (Fig. 3(D)). PVOI captures the linearly decreasing  $R_{Rel}$  slope before 700 nm. Statistical analysis showed significance between PV compared to normal myocardium and lesion (Fig. 3(C)).

Human atrial substrates were identified, using the same optical indices as swine. In Fig. 4(A), mean  $R_{Rel}$  of ablated tissue shows similar attributes as swine atrial tissue with a maximum at 710nm, but overall  $R_{Rel}$  amplitude is less prominent. RF ablated  $R'_{Rel}$  also displays a large peak near 680nm and a minimum at 950nm compared to other substrates (Fig. 4(B)). Human normal myocardium and pulmonary vein  $R_{Rel}$  shows similar spectral shape as the swine, but a subtle local minimum is seen near 670nm in the PV  $R_{Rel}$ . The LOI and PVOI equations developed from the swine *ex vivo* data were also statistically different between identified substrates (Fig. 4(C)-(D)). Fibrosis  $R_{Rel}$  shows a strong dip in signal at 600nm and a maximum near 650nm. Other features remained similar to other substrates. Based on the distinctive shape near 600-650nm range, we established a parameter called fibrosis optical index (FOI) and show statistical significance between groups (Fig. 4(E)). FOI is described stated below.

$$FOI = \frac{R_{Rel}(650nm)}{R_{Rel}(600nm)} \quad (3)$$

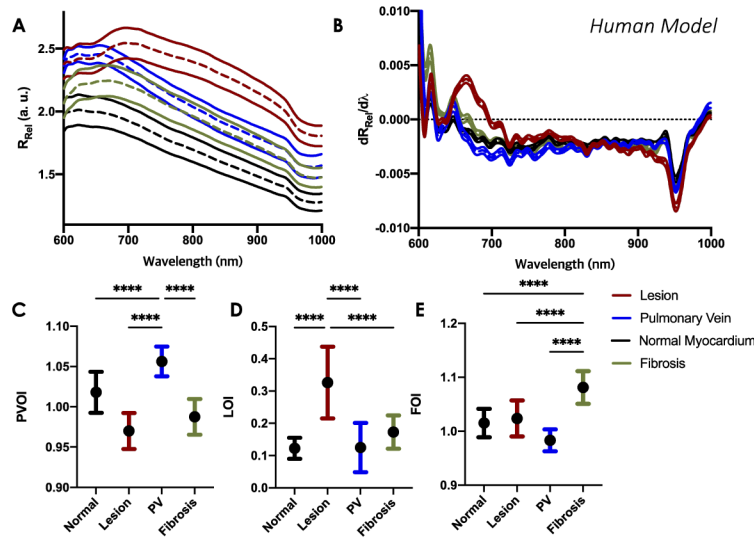


**Fig. 4.** Spectral morphology assessment of human substrates. A: Spectral changes in mean (dotted line) and 95% confidence interval (line) relative reflectance ( $R_{Rel}$ ) in pulmonary vein, normal myocardium, irrigated lesion, and fibrosis. B:  $R'_{Rel}$  curve to emphasize changes in spectral shape. C: Pulmonary vein optical index (PVOI) comparison between substrates. D: Lesion optical index (LOI) comparison between identified substrates. E: Fibrosis optical index (FOI) comparison between substrates. Bars are presented as mean and standard deviation (\*\*\*\*P < 0.0001).

In Fig. 5, 2(D) spatial distribution maps of human left atrium near the left and right superior pulmonary vein are shown. This particular donor experienced atrial fibrillation in the past (Donor #3). In persistent atrial fibrillation, fibrosis areas have been commonly found near the pulmonary vein ostia [43]. Examples of swine 2D spatial distribution maps are shown in the Supplement 1.

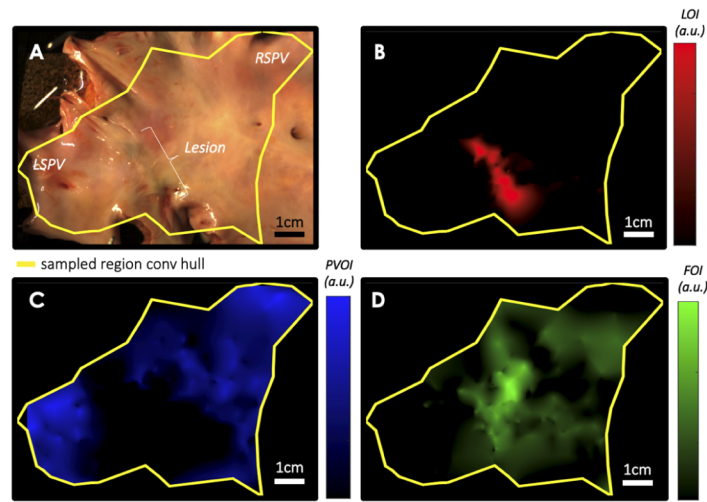


**Fig. 5.** NIRS contrast maps of human donor #3 with atrial fibrillation, with 400 measurements. Five irrigated lesions were placed near the left superior PV. A: raw reference left atrium image captured by CCD camera. B: Spatial distribution of lesion optical index (LOI). Human LOI values were in similar range as swine LOI maps (0.2-0.4). C: Spatial distribution of pulmonary vein optical index (PVOI). Both left and right superior pulmonary veins were highlighted. PVOI values extended into the atrial tissue, which may be due to other tissue types, such as adipose and collagen, which have not been defined yet. D: Spatial distribution of fibrosis optical index (FOI). Fibrosis was detected near the left superior PV and around the lesion sites. Histological correlates of pulmonary vein, lesion and fibrosis are shown in Fig. 9.

#### 2.4. Histopathology and lesion assessment

After NIRS substrate mapping, hearts ( $n_{\text{swine}} = 10$ ,  $n_{\text{human}} = 5$ ) were fixed in formalin for histopathology. Then, tissue from the imaged areas, lesion sites, and pulmonary vein sleeves were cut into blocks. These samples were stained in hematoxylin and eosin (H&E) and Masson's trichrome. A Leica SCN400 (Leica Microsystems, Wetzlar, Germany) slide scanner under 40X magnification was used to digitize histology slides. After, the locations of histology slides were matched by camera reference images of tissue specimen. Stained samples were analyzed using Aperio ImageScope (Leica Biosystems, Buffalo Grove, IL, USA) by a board-certified pathologist. In swine H&E and trichrome stained atrial samples, lesion, normal myocardium, and pulmonary veins were identified. In human stained samples, we also identified areas with adipose and fibrosis within the myocardium. Lesion depth was determined by manual segmentation of histology images within MATLAB. Additionally, lesion depth percentage was derived by measuring the amount of ablated myocardial tissue relative to the total tissue thickness. However, adipose was excluded from the classification model because of small sample size. The remaining two swine hearts were stained in 2,3,5-Triphenyl-2H-tetrazolium chloride (TTC), where lesions stain white and untreated tissue stains red. Lesions were dissected in half and submerged in TTC for 40 minutes at room temperature. Stained samples were analyzed using digitized camera images. Within this study, the average lesion depth measured at the center of the lesion was 1.05 mm, and an average tissue thickness of 1.17 mm. The maximum lesion depth was 5 mm and maximum tissue thickness was 5.14 mm.

### 2.5. OCT imaging protocol and image processing

As a preliminary study, a subsample of NIRS-mapped swine ( $n = 4$ ) and human ( $n = 2$ ) LA were imaged with a benchtop spectral-domain OCT system (TELESTO I, Thorlabs, Dachau, Germany) to correlate microstructural details with NIRS. The system specifications include  $6.5\mu\text{m}$  axial resolution,  $15\mu\text{m}$  lateral resolution, and  $2.51\text{ mm}$  axial imaging range in air. The center wavelength and bandwidth of the system was  $1325\text{ nm}$  and  $150\text{ nm}$ , respectively. Each image volume was taken at  $28\text{kHz}$  A-scan acquisition rate and consisted of  $800 \times 800 \times 512$  voxels, which corresponded to  $8.00 \times 8.00 \times 1.79\text{ mm}$ . All image volumes were taken with some overlaps for volume stitching. 3D image volumes were stitched using a multiband stitching algorithm from previously published work [44]. To improve structural quantification, a contrast enhancement algorithm along with homomorphic filter was implemented on each B-scan [45]. This algorithm suppresses speckle noise and enhances contrast of fibrous tissue features and lesion areas.

### 2.6. Substrate classification

A flow chart of NIRS substrate classification and lesion regression is shown in the [Supplement 1](#). First, a gradient boosting classification algorithm was employed for substrate identification. The gradient boosting algorithm is an ensemble method, which helps to improve the weak outliers and transform them into strong learners for classification. The goal of gradient boosting is to minimize the differentiable loss function in each iteration when forming a new tree. In each iteration, the gradient boosting algorithm uses gradients in the loss function to modify the weights in the data points. A detailed description of the gradient tree boosting algorithm is described in previously published work [46]. To implement the gradient boosting algorithm, eXtreme Gradient Boosting (XGBoost) was used [47].

Total of 6 features were input into the gradient boosting algorithm. In addition to FOI, PVOI, and LOI, we proposed three additional NIRS features called substrate optical indices (SOI). These indices were extracted based on spectral morphology and are listed below:

$$\text{SOI}_1 = \sum_{\lambda_1}^{\lambda_2} (R'_{\text{Rel}}(\lambda) - R'_{\text{Rel}}(661)), [\lambda_1, \lambda_2] = [600\text{nm}, 1000\text{nm}] \quad (4)$$

$$\text{SOI}_2 = \frac{R_{\text{Rel}}(700\text{nm})}{R_{\text{Rel}}(612\text{nm})} \quad (5)$$

$$\text{SOI}_3 = \frac{R_{\text{Rel}}(650\text{nm})}{R_{\text{Rel}}(930\text{nm})} \quad (6)$$

Human and swine measurements were input into the same classifier. A leave-one-out cross-validation scheme was implemented to assess the classifier. The estimated labels at each of the measurement sites were overlayed onto the reference image. Also, the probability distributions were interpolated to display 2D renderings of each substrate.

### 2.7. Lesion regression algorithm

The Gaussian process regression model was employed with 9 optical indices from a previous study with the addition of Eqs. (1)–3, to estimate the extent in depth of tissue injury relative to tissue thickness [41]. The model is a non-parametric Bayesian modelling technique and draws nonlinear relationships between variables [48]. Lesion depth percentage (LD%), was introduced in our previous work to account for variance in myocardial tissue thickness. Lesion depth percentage is represented as a ratio between the amount of ablated tissue and total myocardial thickness. Since the model was based on measurements from the lesion center, additional parameters mentioned were required for accurate assessment of the lesion peripheries. We employed a gaussian process regression model [41] using the LOIs as input variables and lesion dimensions determined from



digitized histological measurements. Lesion depth and depth percentage for spectra collected from catheter-tissue contact and untreated tissue were set to zero. A gaussian process regression model is a supervised learning model where the input and the output are mapped from the training data. It is a non-parametric Bayesian modelling technique that combines prior distribution of known observed data to derive posterior predictive distributions for unknown future data. Optical indices at each measurement sites were interpolated for precise alignment with corresponding measured lesion depth percentage from histology images. The interpolated optical indices were inputted into the algorithm. Finally, the regression model output maps were masked with lesion classified 2D maps to suppress any misclassified sites displayed as 2D maps. Both swine and human lesions were trained for lesion depth percentage estimation.

Lesion depth percentage is represented as a ratio between the amount of ablated tissue and total myocardial thickness. This parameter could serve as an independent parameter of varying myocardial tissue depth to ensure lesion transmural and minimize gaps. Optical indices at each measurement site were interpolated and aligned with corresponding measured lesion depth percentage from histology images. The interpolated optical indices were input into the algorithm. Finally, the regression model output maps were masked with lesion-classified 2D maps from our model. Both swine and human lesions were included in training for lesion depth percentage estimation ( $n_{\text{total}} = 5930$ ).

## 2.8. Statistical analysis

Analysis of variance (ANOVA) with multiple comparison tests were employed to determine the significance of LOI, FOI, and PVOI between groups. Agreement between lesion dimensions and extracted features were quantified using Pearson's correlation coefficient. P-values less than 0.05 were deemed statistically significant. Prism 8 (Graphpad Software, San Diego, California) was used for statistical analyses.

## 3. Results

### 3.1. Swine pre-ablation vs. post-ablation LOI maps and OCT features

NIRS spatial maps and stitched OCT b-scans of pre and post RF ablation were compared in Fig. 6. First, OCT volumes and NIRS measurements were taken on swine LA prior to thermal treatment (Fig. 6(A)) to display ablation induced LOI changes and compared with post-ablation maps (Fig. 6(B)). Five lesions were generated on the specimen with one incidence of steam-pop. Pre-ablation (Fig. 6(C)) and post-ablation (Fig. 6(D)) NIRS maps are shown in same LOI scale ( $\text{LOI} > 0.2$ ). As expected, the lesion optical index was close to zero in the pre-ablation map. In the post-ablation map, lesions and overtreated sites were detected with increased LOI values.

Following NIRS mapping, microstructural details of normal tissue and lesions were examined with OCT. OCT volumes were denoised and pre-processed with our contrast enhancement algorithm. In Fig. 6(E), *en face* plane (x and y dimensions) at 0.25 mm from the tissue surface of a normal site shows myocardial muscle fibers. Likewise, an OCT B-scan (x and z dimensions) of a pre-ablated site also revealed myocardial muscle fibers underneath the thin endocardium, shown in Fig. 6(F). Following RF ablation, the *en face* image of the same location displayed increased backscattering and without myocardial fibers at the lesion location. In the post-ablated OCT B-scan, myocardial muscle fibers were replaced by high intensity features at lesion locations (Fig. 6(H)). Furthermore, disruptions (cavities) within the myocardium were observed.

### 3.2. Gradient boosting classification results

A substrate classification model was trained to identify tissue types using 12 swine hearts and 5 human hearts. Tissue substrates were segmented based on trichrome histology and raw reference images. Measurement sites that fell within the segmentations were labelled. Total

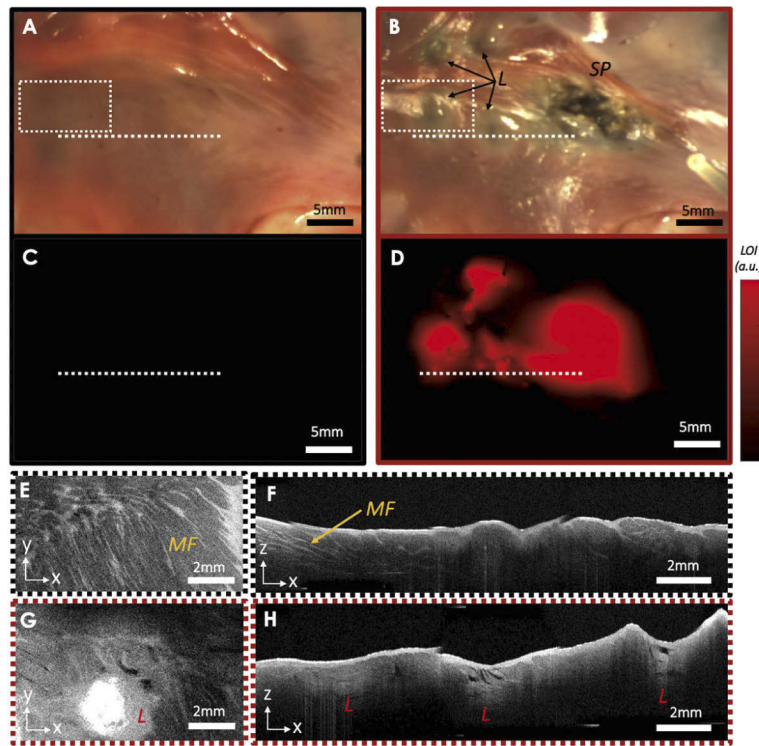


**Fig. 6.** Pre-ablation and post-ablation comparison with NIRS spatial maps and benchtop OCT benchtop volume images. A: Raw reference left atrium image before ablation. B: Raw reference left atrium image after ablation. Total of 5 lesions created with one steam-pop. C shows pre-ablation and D shows post-ablation LOI distribution maps under the same scale. E: *En face* pre-ablation OCT images at the lesion location. F: Pre-ablation OCT b-scan corresponding white dashed line in C and D. Myocardial fibers are shown. G: *En face* post-ablation OCT images at the lesion location. H: Post-ablation OCT b-scan corresponding white dashed line in C and D.

labelled acquisition points for four classes were as follows: normal myocardium ( $n = 1963$ ), lesion ( $n = 942$ ), pulmonary vein ( $n = 747$ ), and fibrosis ( $n = 224$ ). Compared to other classes, the fibrosis class consisted of a smaller size dataset because it was only present in diseased human tissue. The confusion matrix was evaluated by 10-fold cross validation of the total dataset (Fig. 7). The model achieved an overall error of 8.82%.

Representative classification results for swine and human LA are shown in Fig. 8 and Fig. 9, respectively. Interpolated probability distributions of lesion (red) and pulmonary vein (blue) of swine LA were overlaid in Fig. 8(B). In Fig. 8(C)-(D), classifications and trichrome histology were compared and validated. Lesions and the pulmonary vein were clearly shown and confirmed by histological correlates.

A 2D substrate map of human heart classification result is shown in Fig. 9(B). Regions around LSPV and RSPV are well-defined on the classification composite overlay of pulmonary vein. The location of lesion sets was identified and was surrounded by fibrotic tissue. Fibrosis exists within the lesion and near the edges in trichrome histology image (Fig. 9(D)). Fibrosis classifications confirm NIRS is sensitive to fibrotic tissue beneath the endocardium (Fig. 9(E)). While fibrosis is concentrated near the lesion sets, two small regions are also classified as fibrotic tissue to the left of RSPV. This may be attributed to low sampling in that region. Densely sampled regions render

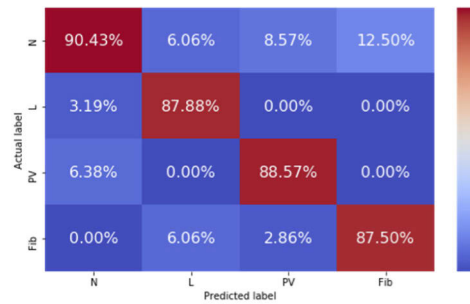


**Fig. 7.** Confusion matrix for gradient boosting classification model for normal (N), lesions (L), pulmonary vein (PV) and fibrosis (Fib) using spectra from both swine and human hearts.

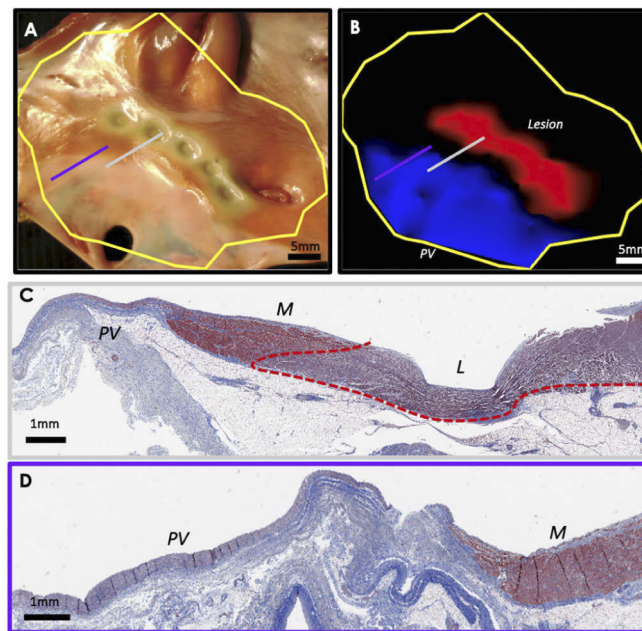


**Fig. 8.** Classification probability distribution map validation with corresponding trichrome histology in swine LA. A: Raw reference swine LA image enclosed by convex hull of measurement sites. B: classification probability distribution overlay of lesion and pulmonary vein. C: corresponding trichrome histology cross-section showing transition from pulmonary vein to lesion. Red dotted lines show lesion boundaries D: corresponding trichrome histology cross-section showing transition from pulmonary vein to myocardium. (M = myocardium, PV = pulmonary vein, L = lesion). Generation of optical index maps shown in [Visualization 1](#).

finer details of fibrosis. NIRS contrast parameters identified general regions of various tissue substrates. Classification model results discriminated each class and showed clear boundaries between substrate classes.

### 3.3. Regression results

The NIRS lesion optical index (LOI) based Gaussian process regression model for predicted lesion depth percentage (LD%) and actual values is shown in Fig. 10. The model was evaluated by root mean squared error (RMSE) and Pearson's correlation coefficients (R). Predicted lesion

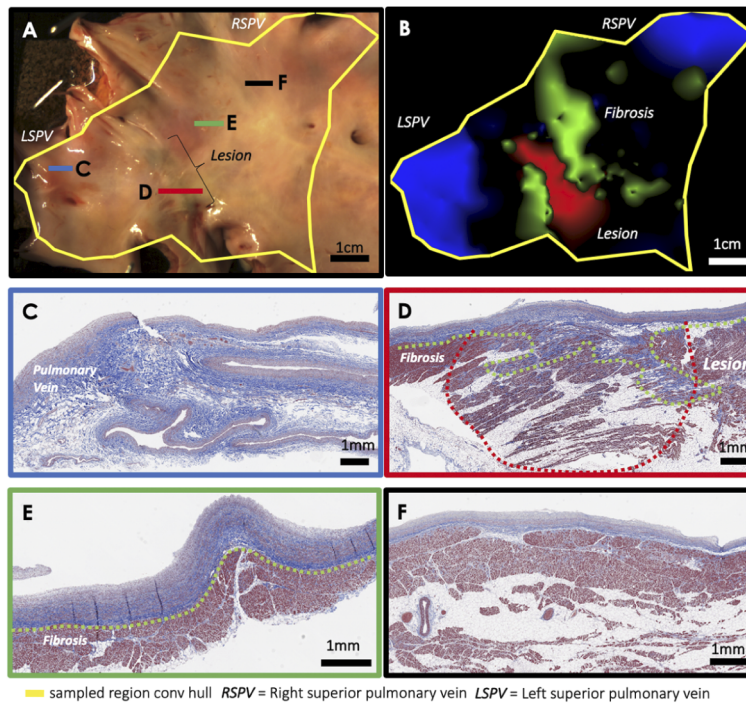


**Fig. 9.** Example classification probability distribution map validation with corresponding trichrome histology for a human LA. Blue, red, green, black corresponds to pulmonary vein, lesion, fibrosis, and normal tissue, respectively. A: Raw reference human LA image enclosed by a convex hull of measurement sites. B: classification probability distribution overlay of lesion, pulmonary vein, and fibrosis. Fibrosis is present around lesion sites, confirmed in D. C: corresponding trichrome histology cross-section of left superior pulmonary vein. D: corresponding trichrome histology cross-section of lesion site. Within the lesion, fibrosis is distributed, shown in dotted green line. E: Fibrosis trichrome histology cross-section shows fibrosis present between the endocardium and myocardium. F: Normal tissue trichrome histology shows smooth transition between endocardium to myocardium.

depth percentage linearly corresponded with actual measurements from trichrome histology measurements (Pearson's  $R = 0.984$ ,  $RMSE = 3.53\%$ ).

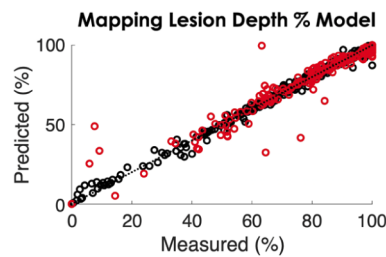


**Fig. 10.** Comparison between model predictions and measured lesion depth percentage (LD%). Both human and swine depth measurements were included. Black circles show training results; red circles correspond to test set samples.



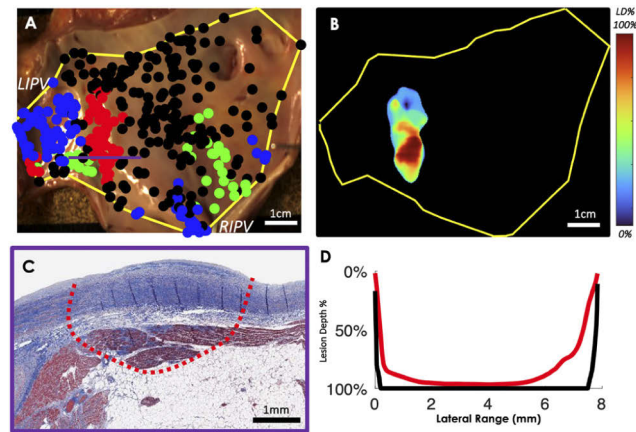


**Fig. 11.** Lesion depth percentage assessment in human left atrium. A: shows classification results at each measurement sites (blue = pulmonary vein, red = lesion, black = normal myocardium, green = fibrosis). B: represents estimated lesion depth percentage results. Within the ablation line, the lower lesions are transmural, and the remaining are superficial. C: Trichrome histology confirms deep transmural lesions at the yellow dashed line. D: Overlay of estimated (red) and actual lesion depth percentage (black) measurements.

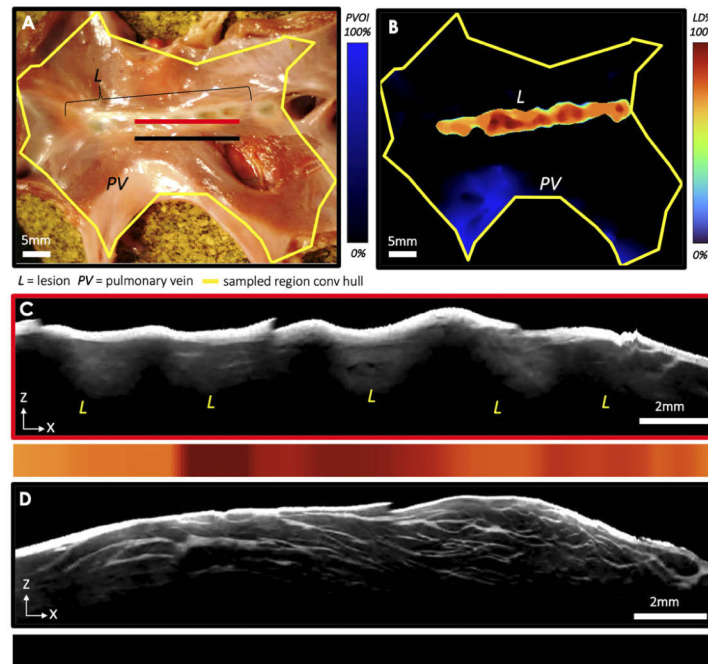


**Fig. 12.** OCT b-scan corresponding to NIRS lesion depth percentage results in swine left atrial tissue. A: Reference image of swine left atrium with irrigated lesion line near the pulmonary vein. B: Overlay of both classified pulmonary vein (blue) and lesion depth percentage estimation (red). C: Contrast enhanced OCT b-scan at ablated site shows five lesions. Estimated lesion depth percentage of lesion (red) site corresponding to red line shown in A. D: Contrast enhanced OCT b-scan at non-ablated site (black line in A) shows muscle fibers. Estimated lesion depth of normal (black) site predicted zero depth percentage.



### 3.4. Lesion depth percentage 2D spatial map

The classification and regression models were evaluated on both swine and human left atrium and interpolated as 2D spatial maps. A representative map of a healthy swine LA is shown in the Supplement 1. In Fig. 11, a human LA near the left and right inferior pulmonary vein with six lesions is shown. The classified map shows lesions created near the left inferior pulmonary vein (LIPV). Also, fibrosis is concentrated near the right inferior pulmonary vein (RIPV) (green). Partial-thickness treatment was predicted for lesions in the upper half of the set, and transmural in the bottom half. The degree of lesion transmural was confirmed by trichrome histology. Figure 11(C) demonstrates transmurally ablated myocardium. Predicted lesion depth showed strong agreement with depth measured in histology (Fig. 11(D)). A small discrepancy is observed between lesion measurements and predicted results in both swine and human. The predicted results slightly underestimate the extent of injury. Errors could result from segmentation, since depth percentage is calculated from manual segmentations. Furthermore, errors could arise from NIRS sample volume at edges of lesions, which may be partially sampling adjacent unablated tissue.

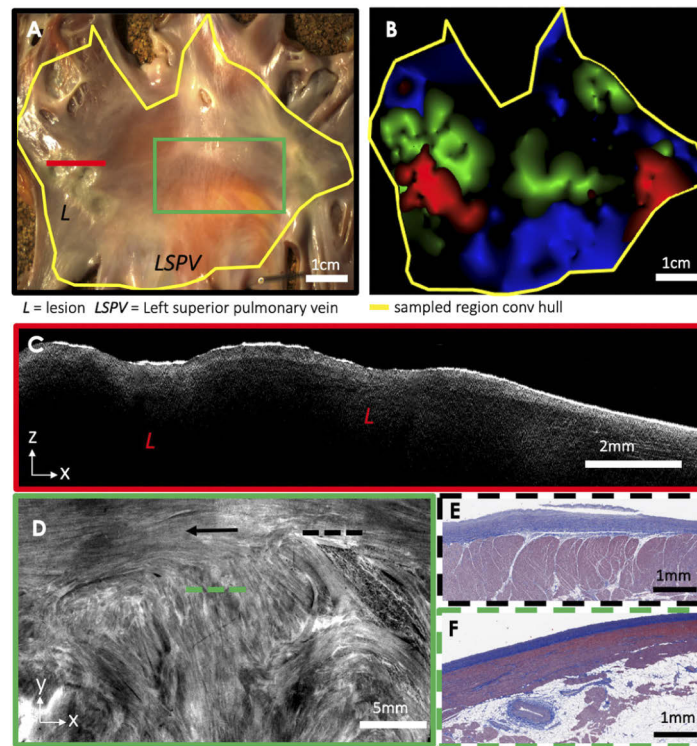


**Fig. 13.** OCT images corresponding to NIRS classified structural substrate results in human left atrial tissue. A: Reference image of swine left atrium with irrigated lesion line near the pulmonary vein. B: Overlay of pulmonary vein, lesion and fibrosis classification. C: Contrast enhanced OCT B-scan corresponding to lesion location. Thick endocardium in human LA prevents OCT from locating lesions in the B-scan. D: *En face* OCT image of fibrosis region shows bright interweaved fibers (fibrosis) in the middle. Green arrows mark signs of fibrosis. Untreated normal sites show collagen fibers, pointed in black arrows. E: Histology image of normal myocardium (black dashed line) for comparison. F: Histology image of fibrosis tissue (green dashed line). Compared to normal myocardium, fibrotic tissue (blue-stained) is seen inside the endocardium and myocardium.

### 3.5. OCT comparison with NIRS

OCT volumes were acquired of swine and human LA to compare microstructural details with NIRS measurements. In Fig. 12(A), swine LA with a set of 8 lesions is shown. Lesion and pulmonary vein locations are well-represented in the composite overlay of classified PV and predicted LD% (Fig. 12(B)). The predicted LD% showed strong agreement with histological measurements and estimated 100% transmural in the middle and gaps around the periphery. In Fig. 12(C)-(D), a contrast enhanced OCT B-scan image and a predicted lesion depth percentage linear map are compared. In Fig. 12(C), the NIRS depth percentage estimation shows lesions ablated with unablated tissue underneath the lesions. Within OCT images, locations of the ablation lesions. However, lesion size could not be measured due to inherent depth limitations. In Fig. 12(D), a contrast enhanced OCT B-scan of an adjacent non-ablated site (black line) shows presence of myocardial muscle fibers. In swine samples, OCT adds significant value to microstructural identification, such as general lesion locations and myocardial muscle fibers. In Fig. 13, OCT and NIRS is compared in human tissue. Two sets of lesions were created in the human left atrium (Fig. 13(A)). Figure 13(B) shows substrate classification of identified classes (PV, fibrosis, and lesions). Lesions on the far right and left are clearly defined with our classification model. In Fig. 13(C), OCT B-scan of right lesion set is shown. Contrarily to swine OCT images, lesion locations are difficult to identify, and microstructural details are not characterized in thicker endocardium. The endocardium is highly backscattering with a gradual intensity fall-off when the endocardium is thicker than the penetration depth. In areas of thin endocardium, enface OCT image showed presence of myocardial fibers and fibrosis. In Fig. 13(D), high density of fibrosis was characterized by increased backscattering and change in texture around the pulmonary vein sleeve.

## 4. Discussion

In this work, we developed a combined NIRS-integrated RFA catheter for atrial substrate mapping on *ex vivo* swine and human samples. We proposed a classification algorithm for pulmonary vein, lesion, and fibrosis using optically-derived parameters based on endogenous tissue spectral signatures. Using position tracking and interpolation algorithms, tissue structures were reconstructed in 2D spatial maps for visualization. Additionally, a lesion depth percentage model was introduced to predict the extent of tissue necrosis.

The proposed NIRS contrast parameters for structural substrates were empirically derived. With near-infrared spectroscopy, light interaction with the tissue optical properties can reveal underlying tissue microstructures and biomolecular composition [49]. Previous studies have also shown increase in reflectance in thermally coagulated tissues within non-irrigated lesions [37,39]. In our group, irrigated lesions were quantified real-time during ablation therapy using near-infrared spectroscopy on *ex vivo* and preliminary *in vivo* swine models [41].

The classification model accurately predicted pulmonary vein sleeves, lesion, and fibrosis location (>87%) with our optical indices. Detailed evaluation of anatomical location of the sleeves is critical for a successful pulmonary vein isolation procedure. Studies have suggested existence of abnormal triggers located within the PVs [50]. Also, the arrangement and number of pulmonary vein ostia is unpredictable among patients [51,52]. Both myocardium and venous media consists of cardiomyocytes, a form of muscle cell. The main absorbers are water and hemoglobin, and the absorption coefficient is high at 633 nm [53]. Although myocytes are present in the pulmonary vein, a higher concentration is seen in myocardial tissue. Thus, we observed a decrease in  $R_{Rel}$  amplitude in 600-670 nm range. Pulmonary vein  $R_{Rel}$  decreased linearly throughout the spectrum since it was less affected by the absorption peak of cardiomyocytes. In human samples, pulmonary vein  $R_{Rel}$  showed similar spectral morphology as normal myocardial tissue because the endocardium extends into the pulmonary vein sleeve. Yet, PVOI showed statistical differences compared to other tissue types. Human pulmonary vein sleeves carry

highly complex arrangement of myofiber bundles with mixture of fat and fibrous tissue. Further studies are needed to assess the complex architecture within the pulmonary veins. Since fibrosis is collagen-rich, FOI was identified by observing the collagen absorption spectra. Absorption coefficient below 650 nm range was higher than the near-infrared [54]. This is consistent with our finding in Fig. 4(A) (green). We observed a decrease in  $R_{Rel}$  amplitude near 600-650 nm in the fibrosis class as it highlights the underlying collagen deposition within fibrotic tissue. The three substrates identified in this work are only a small subset in the complex heterogeneous atria. Future studies will aim to locate other tissue types, such as adipose tissue.

In addition, our model demonstrated accurate predictions for assessing lesion quality of irrigated RFA lesions ( $R = 0.984$ ). Lesion depth analysis was not included in this study since significant tissue deformation and tears were seen in histology correlates. Instead, we believe that lesion depth percentage represent the ultimate objective of reaching transmural by measuring lesion depth relative to the total tissue thickness. One of the limitations for assessing lesion is assessing the degree of tissue necrosis. In some cases, heavily treated sites show tissue injury beyond the myocardium or appear much darker than other lesions. Therefore, quantitative metrics for myocardial tissue necrosis needs to be further studied.

Lastly, we demonstrated that NIRS and OCT are complimentary. NIRS was superior in detecting lesions in areas of thicker endocardium and predicting lesion size. OCT enabled microstructural imaging of various tissue structure. In Fig. 6, tissue disruptions were observed in an OCT B-scan, which may be a precursor of overtreatment. Also, the orientation and density of myocardial fibers and fibrosis were seen in detail with OCT (Fig. 13). The combination of NIRS and OCT could provide greater understanding of tissue damage and underlying complex cardiac substrates. The combined modality would require a catheter-based OCT system.

Future studies will be carried out to address current limitations of our study design. First, lesion optical indices were based on acute irrigated lesions. Scar tissue from remodeled lesions have yet to be measured. Future work will also be aimed at translating our technology *in vivo*. Previous work has shown that *ex vivo* optical spectral optical indices can be used to differentiate *in vivo* ablation lesions from unablated tissue, within healthy swine within the right ventricle [41]. For further validation of substrates such as fibrosis, an animal model with cardiovascular disease will be needed for *in vivo* validation. The camera tracking was a temporary scheme for *ex vivo* analysis, within a flattened sample preparation. Future studies will utilize magnetic field or impedance-based tracking system to enable three-dimensional position tracking in the presence of blood and motion. The camera tracking is a temporary scheme for *ex vivo* analysis. In the future, we envision a combined NIRS and OCT optical probe that is combined with electroanatomical mapping. This will enable further studies to directly compare electrogram voltage measurements at our measurement sites to tissue composition and architecture.

## 5. Conclusion

An intraoperative NIRS-combined RF ablation/mapping catheter was developed for assessing atrial structural substrates and lesion transmural. The resulting model identified pulmonary vein, lesion, and fibrosis with direct optical measurements. The proposed optical method has the potential to improve treatment efficacy by quantifying structural substrates and validating durable lesions alongside current electroanatomical mapping system.

**Funding.** Columbia University (STAR Award); Division of Chemical, Bioengineering, Environmental, and Transport Systems (1454365); National Heart, Lung, and Blood Institute (4DP2HL127776-02, 5R01HL149369).

**Disclosures.** Dr. Ziv has consulted for Biosense Webster and is the recipient of a research grant from Biosense Webster. Dr. Saluja is a consultant for Abbott.

**Data availability.** Data underlying the results presented in this paper are not publicly available at this time but may be obtained from the authors upon reasonable request.

**Supplemental document.** See [Supplement 1](#) for supporting content.

## References

1. M. Haïssaguerre, P. Jaïs, D. C. Shah, A. Takahashi, M. Hocini, G. Quiniou, S. Garrigue, A. Le Mouroux, P. Le Métayer, and J. Clémenty, "Spontaneous initiation of atrial fibrillation by ectopic beats originating in the pulmonary veins," *N. Engl. J. Med.* **339**(10), 659–666 (1998).
2. H. Nathan and M. Eliakim, "The junction between the left atrium and the pulmonary veins: an anatomic study of human hearts," *Circulation* **34**(3), 412–422 (1966).
3. S. A. Chen, M. H. Hsieh, C. T. Tai, C. F. Tsai, V. S. Prakash, W. C. Yu, T. L. Hsu, Y. A. Ding, and M. S. Chang, "Initiation of atrial fibrillation by ectopic beats originating from the pulmonary veins: Electrophysiological characteristics, pharmacological responses, and effects of radiofrequency ablation," *Circulation* **100**(18), 1879–1886 (1999).
4. A. Verma, C. Jiang, T. R. Betts, J. Chen, I. Deisenhofer, R. Mantovan, L. Macle, C. A. Morillo, W. Haverkamp, R. Weerasooriya, J.-P. Albenque, S. Nardi, E. Menardi, P. Novak, and P. Sanders, "Approaches to Catheter Ablation for Persistent Atrial Fibrillation," *N. Engl. J. Med.* **372**(19), 1812–1822 (2015).
5. A. N. Ganesan, N. J. Shipp, A. G. Brooks, P. Kuklik, D. H. Lau, H. S. Lim, T. Sullivan, K. C. Roberts-Thomson, and P. Sanders, "Long-term outcomes of catheter ablation of atrial fibrillation: a systematic review and meta-analysis," *J. Am. Heart Assoc.* **2**(2), e004549 (2013).
6. J. M. Kalman, P. M. Kistler, and A. J. Taylor, "Cardiac magnetic resonance imaging to detect non-contiguous scar following atrial fibrillation ablation: Identifying our knowledge gaps," *Eur. Heart J.* **35**(22), 1436–1438 (2014).
7. G. Caixal, F. Alarcón, T. F. Althoff, M. Nuñez-García, E. M. Benito, R. Borràs, R. J. Perea, S. Prat-González, P. Garre, D. Soto-Iglesias, C. Gunturitz, J. Cozzari, M. Linhart, J. M. Tolosana, E. Arbelo, I. Roca-Luque, M. Sitges, E. Guasch, and L. Mont, "Accuracy of left atrial fibrosis detection with cardiac magnetic resonance: correlation of late gadolinium enhancement with endocardial voltage and conduction velocity," *Europace* **23**(3), 380–388 (2021).
8. S. Nattel, B. Burstein, and D. Dobrev, "Atrial remodeling and atrial fibrillation: mechanisms and implications," *Circ. Arrhythm. Electrophysiol.* **1**(1), 62–73 (2008).
9. N. Akoum and N. Marrouche, "Assessment and impact of cardiac fibrosis on atrial fibrillation," *Curr. Cardiol. Rep.* **16**(8), 518 (2014).
10. A. Xintarakou, S. Tzeis, S. Psarras, D. Asvestas, and P. Vardas, "Atrial fibrosis as a dominant factor for the development of atrial fibrillation: Facts and gaps," *Europace* **22**(3), 342–351 (2020).
11. M. Das, J. J. Loveday, G. J. Wynn, S. Gomes, Y. Saeed, L. J. Bonnett, J. E. P. Waktare, D. M. Todd, M. C. S. Hall, R. L. Snowden, S. Modi, and D. Gupta, "Ablation index, a novel marker of ablation lesion quality: Prediction of pulmonary vein reconnection at repeat electrophysiology study and regional differences in target values," *Europace* **19**(5), 775–783 (2017).
12. F. Ouyang, D. Bänsch, S. Ernst, A. Schaumann, H. Hachiya, M. Chen, J. Chun, P. Falk, A. Khanedani, M. Antz, and K.-H. Kuck, "Complete isolation of left atrium surrounding the pulmonary veins," *Circulation* **110**(15), 2090–2096 (2004).
13. M. Masuda, M. Fujita, O. Iida, S. Okamoto, T. Ishihara, K. Nanto, T. Kanda, T. Tsujimura, Y. Matsuda, S. Okuno, T. Ohashi, A. Tsuji, and T. Mano, "Left atrial low-voltage areas predict atrial fibrillation recurrence after catheter ablation in patients with paroxysmal atrial fibrillation," *Int. J. Cardiol.* **257**, 97–101 (2018).
14. A. Verma, O. M. Wazni, N. F. Marrouche, D. O. Martin, F. Kilicaslan, S. Minor, R. A. Schweikert, W. Saliba, J. Cummings, J. D. Burkhardt, M. Bhargava, W. A. Belden, A. Abdul-Karim, and A. Natale, "Pre-existent left atrial scarring in patients undergoing pulmonary vein antrum isolation: An independent predictor of procedural failure," *J. Am. Coll. Cardiol.* **45**(2), 285–292 (2005).
15. M. El Haddad, P. Taghji, T. Philips, M. Wolf, A. Demolder, R. Choudhury, S. Knecht, Y. Vandekerckhove, R. Tavernier, H. Nakagawa, and M. Duytschaever, "Determinants of acute and late pulmonary vein reconnection in contact force-guided pulmonary vein isolation," *Circ. Arrhythmia Electrophysiol.* **10**(4), e004867 (2017).
16. G. Rozen, L. Ptaszek, I. Zilberman, K. Cordaro, E. K. Heist, C. Beeckler, A. Altmann, Z. Ying, Z. Liu, J. N. Ruskin, A. Govari, and M. Mansour, "Prediction of radiofrequency ablation lesion formation using a novel temperature sensing technology incorporated in a force sensing catheter," *Hear. Rhythm* **14**(2), 248–254 (2017).
17. F. Squara, D. G. Latcu, Y. Massaad, M. Mahjoub, S. S. Bun, and N. Saoudi, "Contact force and force-time integral in atrial radiofrequency ablation predict transmural lesions," *Europace* **16**(5), 660–667 (2014).
18. A. Codreanu, F. Odille, E. Aliot, P.-Y. Marie, I. Magnin-Poull, M. Andronache, D. Mandry, W. Djaballah, D. Régent, J. Felblinger, and C. de Chillou, "Electroanatomic Characterization of Post-Infarct Scars," *J. Am. Coll. Cardiol.* **52**(10), 839–842 (2008).
19. C. McGann, N. Akoum, A. Patel, E. Kholmovski, P. Revelo, K. Damal, B. Wilson, J. Cates, A. Harrison, R. Ranjan, N. S. Burgon, T. Greene, D. Kim, E. V. R. DiBella, D. Parker, R. S. MacLeod, and N. F. Marrouche, "Atrial fibrillation ablation outcome is predicted by left atrial remodeling on MRI," *Circ. Arrhythmia Electrophysiol.* **7**(1), 23–30 (2014).
20. N. Muselimyan, H. Asfour, and N. Sarvazyan, "Key factors behind autofluorescence changes caused by ablation of cardiac tissue," *Sci. Rep.* **10**(1), 15369 (2020).
21. M. Mercader, L. Swift, S. Sood, H. Asfour, M. Kay, and N. Sarvazyan, "Use of endogenous NADH fluorescence for real-time in situ visualization of epicardial radiofrequency ablation lesions and gaps," *Am. J. Physiol. - Hear. Circ. Physiol.* **302**(10), H2131–H2138 (2012).



22. D. A. Gil, L. M. Swift, H. Asfour, N. Muselimyan, M. A. Mercader, and N. A. Sarvazyan, "Autofluorescence hyperspectral imaging of radiofrequency ablation lesions in porcine cardiac tissue," *J. Biophotonics* **10**(8), 1008–1017 (2017).
23. T. H. Lye, C. C. Marboe, and C. P. Hendon, "Imaging of subendocardial adipose tissue and fiber orientation distributions in the human left atrium using optical coherence tomography," *J. Cardiovasc. Electrophysiol.* **30**(12), 2950–2959 (2019).
24. V. Tiporlini, S. Ahderom, P. Pratten, and K. Alameh, "Advanced fully integrated radiofrequency/optical-coherence-tomography irrigated catheter for atrial fibrillation ablation," *J. Biophotonics* **14**(2), e202000243 (2021).
25. X. Zhao, X. Fu, C. Blumenthal, Y. T. Wang, M. W. Jenkins, C. Snyder, M. Arruda, and A. M. Rollins, "Integrated RFA/PSOCT catheter for real-time guidance of cardiac radio-frequency ablation," *Biomed. Opt. Express* **9**(12), 6400–6411 (2018).
26. C. P. Fleming, K. J. Quan, H. Wang, G. Amit, and A. M. Rollins, "In vitro characterization of cardiac radiofrequency ablation lesions using optical coherence tomography," *Opt. Express* **18**(3), 3079 (2010).
27. X. Yao, Y. Gan, Y. Ling, C. C. Marboe, and C. P. Hendon, "Multicontrast endomyocardial imaging by single-channel high-resolution cross-polarization optical coherence tomography," *J. Biophotonics* **11**(4), e201700204 (2018).
28. D. Liang, D. Taeschler, C. Goepfert, P. Arnold, A. Zurbuchen, R. Sweda, T. Reichlin, H. Tanner, L. Roten, and A. Haeblerlin, "Radiofrequency ablation lesion assessment using optical coherence tomography – a proof-of-concept study," *J. Cardiovasc. Electrophysiol.* **30**(6), 934–940 (2019).
29. C. P. Fleming, N. Rosenthal, and A. M. Rollins, "First in vivo real-time imaging of endocardial radiofrequency ablation by optical coherence tomography : implications on safety and the birth of “ electro-structural ” substrate-guided ablation," *J. Innov. Card. Rhythm Manag.* **2**, 199–201 (2011).
30. Y. Gan, D. Tsay, S. B. Amir, C. C. Marboe, and C. P. Hendon, "Automated classification of optical coherence tomography images of human atrial tissue," *J. Biomed. Opt.* **21**(10), 101407 (2016).
31. D. Herranz, J. Lloret, S. Jiménez-Valero, J. L. Rubio-Guivernau, and E. Margallo-Balbás, "Novel catheter enabling simultaneous radiofrequency ablation and optical coherence reflectometry," *Biomed. Opt. Express* **6**(9), 3268 (2015).
32. H. Wang, W. Kang, T. Carrigan, A. Bishop, N. Rosenthal, M. Arruda, and A. M. Rollins, "In vivo intracardiac optical coherence tomography imaging through percutaneous access: toward image-guided radio-frequency ablation," *J. Biomed. Opt.* **16**(11), 110505 (2011).
33. S. Iskander-Rizk, P. Kruizinga, R. Beurskens, G. Springeling, F. Mastik, N. M. S. de Groot, P. Knops, A. F. W. van der Steen, and G. van Soest, "Real-time photoacoustic assessment of radiofrequency ablation lesion formation in the left atrium," *Photoacoustics* **16**, 100150 (2019).
34. Ç. Özsoy, M. Floryan, X. L. Deán-Ben, and D. Razansky, "Endocardial irrigated catheter for volumetric optoacoustic mapping of radio-frequency ablation lesion progression," *Opt. Lett.* **44**(23), 5808–5811 (2019).
35. R. P. Singh-moon, S. Y. Park, D. M. Song Cho, A. Vaidya, C. C. Marboe, E. Y. Wan, and C. P. Hendon, "Feasibility of near-infrared spectroscopy as a tool for anatomical mapping of the human epicardium," *Biomed. Opt. Express* **11**(8), 4099–4109 (2020).
36. S. Y. Park, R. P. Singh-Moon, E. Y. Wan, and C. P. Hendon, "Towards real-time multispectral endoscopic imaging for cardiac lesion quality assessment," *Biomed. Opt. Express* **10**(6), 2829–2846 (2019).
37. S. G. Demos and S. Sharareh, "Real time assessment of RF cardiac tissue ablation with optical spectroscopy," *Opt. Express* **16**(19), 15286 (2008).
38. J. Swartling, S. Pålsson, P. Platonov, S. B. Olsson, and S. Andersson-Engels, "Changes in tissue optical properties due to radio-frequency ablation of myocardium," *Med. Biol. Eng. Comput.* **41**(4), 403–409 (2003).
39. R. P. Singh-Moon, C. C. Marboe, and C. P. Hendon, "Near-infrared spectroscopy integrated catheter for characterization of myocardial tissues: preliminary demonstrations to radiofrequency ablation therapy for atrial fibrillation," *Biomed. Opt. Express* **6**(7), 2494 (2015).
40. R. P. Singh-Moon, X. Yao, V. Iyer, C. Marboe, W. Whang, and C. P. Hendon, "Real-time optical spectroscopic monitoring of nonirrigated lesion progression within atrial and ventricular tissues," *J. Biophotonics* **12**(4), 1 (2019).
41. S. Y. Park, R. Singh-Moon, H. Yang, D. Saluja, and C. Hendon, "Quantification of irrigated lesion morphology using near-infrared spectroscopy," *Sci. Rep.* **11**(1), 20160 (2021).
42. P. Jaïs, M. Haïssaguerre, D. C. Shah, A. Takahashi, M. Hocini, T. Laverigne, S. Lafitte, A. Le Mouroux, B. Fischer, and J. Clémenty, "Successful irrigated-tip catheter ablation of atrial flutter resistant to conventional radiofrequency ablation," *Circulation* **98**(9), 835–838 (1998).
43. D. Corradi, S. Callegari, S. Benussi, S. Nascimbene, P. Pastori, S. Calvi, R. Maestri, E. Astorri, C. Pappone, and O. Alfieri, "Regional left atrial interstitial remodeling in patients with chronic atrial fibrillation undergoing mitral-valve surgery," *Virchows Arch.* **445**(5), 498–505 (2004).
44. T. H. Lye, V. Iyer, C. C. Marboe, and C. P. Hendon, "Mapping the human pulmonary venoatrial junction with optical coherence tomography," *Biomed. Opt. Express* **10**(2), 434–448 (2019).
45. J. P. McLean, S. Fang, G. Gallos, K. M. Myers, and C. P. Hendon, "Three-dimensional collagen fiber mapping and tractography of human uterine tissue using OCT," *Biomed. Opt. Express* **11**(10), 5518–5541 (2020).
46. D. Ruppert, "The elements of statistical learning: data mining, inference, and prediction," *J. Am. Stat. Assoc.* **99**(466), 567 (2004).
47. T. Chen and C. Guestrin, "XGBoost: A scalable tree boosting system," in *Proceedings of the ACM SIGKDD International Conference on Knowledge Discovery and Data Mining* (2016).



48. C. E. Rasmussen, "Gaussian Processes in machine learning," *Lect. Notes Comput. Sci. (including Subser. Lect. Notes Artif. Intell. Lect. Notes Bioinformatics)* (2004).
49. S. L. Jacques, "Optical properties of biological tissues: A review," *Phys. Med. Biol.* **58**(11), R37–R61 (2013).
50. S. Y. Ho, J. A. Cabrera, V. H. Tran, J. Farré, R. H. Anderson, and D. Sánchez-Quintana, "Architecture of the pulmonary veins: relevance to radiofrequency ablation," *Br. Heart J.* **86**(3), 265–270 (2001).
51. T. Akiba, H. Marushima, M. Odaka, J. Harada, S. Kobayashi, and T. Morikawa, "Pulmonary vein analysis using three-dimensional computed tomography angiography for thoracic surgery," *Gen. Thorac. Cardiovasc. Surg.* **58**(7), 331–335 (2010).
52. E. M. Marom, J. E. Herndon, Y. H. Kim, and H. P. McAdams, "Variations in pulmonary venous drainage to the left atrium: implications for radiofrequency ablation," *Radiology* **230**(3), 824–829 (2004).
53. A. N. Bashkatov, E. A. Genina, and V. V. Tuchin, "Optical properties of skin, subcutaneous, and muscle tissues: A review," *J. Innov. Opt. Health Sci.* **04**(01), 9–38 (2011).
54. S. K. V. Sekar, I. Bargigia, A. D. Mora, P. Taroni, A. Ruggeri, A. Tosi, A. Pifferi, and A. Farina, "Diffuse optical characterization of collagen absorption from 500 to 1700nm," *J. Biomed. Opt.* **22**(1), 015006 (2017).